

Understanding the effects of annealing temperature on the mechanical properties of layers in FAI-rich perovskite solar cells

Cite as: AIP Advances 12, 025104 (2022); <https://doi.org/10.1063/5.0078558>

Submitted: 13 November 2021 • Accepted: 12 January 2022 • Published Online: 02 February 2022

O. V. Oyelade,  O. K. Oyewole, Y. A. Olanrewaju, et al.



View Online



Export Citation



CrossMark



Call For Papers!

AIP Advances

SPECIAL TOPIC: Advances in
Low Dimensional and 2D Materials

Understanding the effects of annealing temperature on the mechanical properties of layers in FAI-rich perovskite solar cells

Cite as: AIP Advances 12, 025104 (2022); doi: 10.1063/5.0078558

Submitted: 13 November 2021 • Accepted: 12 January 2022 •

Published Online: 2 February 2022










View Online



Export Citation



CrossMark

O. V. Oyelade,^{1,2} O. K. Oyewole,^{3,4}  Y. A. Olanrewaju,⁵ R. Ichwani,³ R. Koech,⁵  D. O. Oyewole,³ 
S. A. Adeniji,¹  D. M. Sanni,¹  J. Cromwell,⁴  R. A. Ahmed,⁴  K. Orisekeh,⁵ V. C. Anye,⁵
and W. O. Soboyejo^{3,4,a)} 

AFFILIATIONS

¹ Department of Theoretical and Applied Physics, African University of Science and Technology, Km. 10 Airport Road, Galadimawa, P.M.B. 186, Garki-Abuja, Federal Capital Territory, Nigeria

² Department of Physics, Bingham University, Km. 26 Abuja Keffi Express Way, P.M.B. 005, Karu, Nasarawa State, Nigeria

³ Materials Science and Engineering Program, Department of Mechanical Engineering, Worcester Polytechnic Institute, 100 Institute Road, Worcester, Massachusetts 01609, USA

⁴ Department of Mechanical Engineering, Worcester Polytechnic Institute, 100 Institute Road, Worcester, Massachusetts 01609, USA

⁵ Department of Material Science, African University of Science and Technology, Km. 10 Airport Road, Galadimawa, P.M.B. 186, Garki-Abuja, Federal Capital Territory, Nigeria

^{a)} Author to whom correspondence should be addressed: wsoboyejo@wpi.edu. Tel.: +1 508 831 5448 Current address: Program in Materials Science and Engineering, Worcester Polytechnic Institute, 100 Institute Road, Worcester, Massachusetts 01609, USA.

ABSTRACT

This paper uses a combination of experiments and theory to study the effects of annealing temperature on the mechanical properties of hybrid organic–inorganic perovskites (HOIPs). We examined the mechanical (hardness and Young's modulus), microstructural, and surface topography properties of the HOIP film at different annealing temperatures ranging from 80 to 170 °C. A mechanism-based strain gradient (MSG) theory is used to explain indentation size effects in films at different annealing temperatures. Intrinsic film yield strengths and hardness values (deduced from the MSG theory) are then shown to exhibit a Hall–Petch dependence on the inverse square root of the average grain size. The implications of the results are then discussed for the design of mechanically robust perovskite solar cells.

© 2022 Author(s). All article content, except where otherwise noted, is licensed under a Creative Commons Attribution (CC BY) license (<http://creativecommons.org/licenses/by/4.0/>). <https://doi.org/10.1063/5.0078558>

I. INTRODUCTION

Hybrid organic–inorganic perovskites (HOIPs) have emerged as promising energy-related materials for light absorbers in PV cells¹ and emitters in light-emitting diodes (LEDs)² and photodetectors.³ The general formula of HOIPs is ABX₃, where A = CH₃NH₃⁺ (MA⁺), CH(NH₂)₂⁺ (FA⁺), or Cs⁺; B = Pb⁺² or Sn²⁺; and X = I⁻¹, Br⁻¹, or Cl⁻¹. The efficiency of perovskite solar cells (PSCs) has increased drastically above 25%⁴ over the past decade due to the novel electronic and optical,⁵ thermoelectric,⁶ and surface properties of the perovskite absorbers; scalable properties; low

processing-temperature;⁷ tunable and direct bandgaps;⁸ and high extinction coefficients, high carrier mobility, low exciton binding energies, and high absorption over a wide range of wavelengths.⁹ Perovskite materials also have potential for wearable functional devices with great mechanical flexibility and robustness.^{10,11} With the growing interest in HOIPs for deformable devices, the knowledge of their mechanical response to dynamic strain can adequately implement these materials on flexible and stretchable devices.

The understanding of variations in the mechanical properties of HOIP structures that are processed at different annealing

conditions is critical for ultimate device performance and robustness. Annealing temperature influences the structure, morphology, crystallinity, and optoelectrical properties of perovskite films.^{12–17} The annealing process is also critical in the formation of the perovskite film and, consequently, in the power conversion efficiency (PCE) of the assembled devices.¹⁸ Increased annealing temperature can cause inter-diffusion and increased local stresses that can lead to the nucleation of cracks¹⁹ and pinhole formation.

Although research into electrical bands and exciton diffusion pathways has progressed quickly, only a few experimental and theoretical studies have been reported on mechanical properties.^{20–25} The mechanical properties have an impact on the structural phase transition according to current studies of the production of flexible hybrid perovskite solar cells resistant to fatigue—material degradation and mismatch at interfaces, and the consequent lifetime.^{22,26} Several theoretical^{21,27} and experimental^{24,25} calculations have been used to study the mechanical characteristics of organic–inorganic perovskite single crystals. Feng²⁰ used the first-principles method to explore the mechanical characteristics of methylammonium halide perovskites. By monitoring nanoindentation creep and stress relaxation, Reyes-Martinez *et al.*²⁵ were able to determine the time- and rate-dependent mechanical characteristics of HOIPs and inorganic perovskite (IP) single crystals. However, a complete understanding of the mechanical properties of the HOIP films in nano-/micro-scale as a function of different annealing temperatures is yet to emerge. Several thermal annealing temperatures have been used to process perovskite solar cells.^{12,17} It is, therefore, important to understand the mechanical robustness of these perovskite structures that are processed at different annealing temperatures. Motivated by the need to better understand the small-scale mechanical behaviors of HOIPs, nanoindentation experiments have been performed on perovskite structures to ascertain mechanical integrity and robustness.

In this paper, a combined experimental and theoretical approach is used to study micro- to nano-scale contacts in formamidinium-rich perovskite films that are relevant to applications in bendable and wearable perovskite solar cell devices. The perovskite films are processed at different annealing temperatures before relating their mechanical properties to performance characteristics. Contact-induced deformations and the indentation size effects (ISEs) are then studied in the micro- and nano-scale regimes. The observed indentation size effects are explained by considering the role of geometrically necessary dislocations (GNDs) using the mechanism-based strain gradient (MSG) theoretical models by Gao *et al.*²⁸ and Ma and Clarke.²⁹ The intrinsic yield stress/hardness values, extracted from the MSG theory, are shown to exhibit a Hall–Petch dependence on grain size. The Young's moduli are determined using the Oliver–Pharr³⁰ and Hay–Crawford³¹ methods that account for substrate effects. The implications of the results are then discussed for the design of robust PSCs.

II. THEORY

A very comprehensive approach for the determination of the hardness and modulus from depth-sensing indentation load–displacement data was developed by Doerner and Nix³² and

later by Oliver and Pharr.³⁰ The definition of hardness, H , by Meyer was adopted in theory.³² This is given by

$$H = \frac{P_{\max}}{A}, \quad (1)$$

where P_{\max} is the maximum load and A is the projected contact area. The recorded load–displacement data were used to relate the stiffness, S , from the slope of the initial unloading curve to the reduced elastic modulus, E_r ,

$$E_r = \frac{\sqrt{\pi}}{2} \frac{S}{\sqrt{A}}, \quad (2)$$

where S is the contact stiffness corresponding to the slope of the load penetration curve at the beginning of the unloading and E_r is expressed in terms of the elastic moduli (E) and Poisson's ratios (ν) of the indenter (i) and the indented material (im),

$$\frac{1}{E_r} = \frac{1 - \nu_i^2}{E_i} + \frac{1 - \nu_{im}^2}{E_{im}}. \quad (3)$$

The projected contact area A calibrated with the contact depth h_c is given by³³

$$A(h_c) = 24.5h_c^2 + C_1h_c^1 + C_2h_c^{1/2} + \dots + C_8h_c^{1/128}, \quad (4)$$

where C_1 through C_8 are constants.

After accounting for the tip rounding distance, $\xi = 0.75$, for the Berkovich indenter³³ and indentation pileup height h_p ,³⁴ the corrected contact area is calculated as follows:

$$A(h_c) = 24.5(h_c + \xi + h_p)^2 + C_1(h_c + \xi + h_p)^1 + C_2(h_c + \xi + h_p)^{1/2} + \dots + C_8(h_c + \xi + h_p)^{1/128}. \quad (5)$$

Plasticity theories cannot be utilized to explain indentation size effects in submicrometer-thin films where the size effect is evident because no material length scales include the phenomenon. Theories on strain gradient plasticity (SGP)^{28,35} are therefore necessary to explain the size effects. Nix and Gao³⁶ developed a mechanism-based strain gradient (MSG) model to rationalize the indentation size effects. The model expresses the depth dependence of hardness as

$$\left(\frac{H}{H_0}\right)^2 = 1 + \frac{h^*}{h}, \quad (6)$$

where H is the hardness for a given indent depth h , H_0 is the size independent hardness, and h^* is the characteristic length parameter that characterizes the depth dependence of the hardness. This model predicts that the hardness square is linear to the indentation depth reciprocal.

Nix and Gao³⁶ also derived an intrinsic length scale \hat{l} from the MSG model to accommodate the indentation size dependence of hardness with the strain gradient,

$$\left(\frac{\sigma}{\sigma_0}\right)^2 = 1 + \hat{l}\chi, \quad (7)$$

where σ is the effective flow stress in the presence of a gradient, σ_0 is the flow stress in the absence of a gradient, χ is the effective strain

gradient, and \hat{l} is a characteristic material length scale. Equation (7) gives the physical meaning of this characteristic material length scale, \hat{l} , which is a measure of the contribution of the strain gradient to the flow stress.

\hat{l} can be expressed in terms of Burger's vector b and shear modulus μ as

$$\hat{l} = \frac{b}{2} \left(\frac{\mu}{\sigma_0} \right)^2. \quad (8)$$

The relative contributions of statistically stored dislocations (SSDs) and geometrically necessary dislocations (GNDs) were approximated with a model by Ma and Clarke using the Taylor and Tabor relation.³⁷ The strain gradient is the average shear strain Y over an indentation size D .²⁹ The density of GNDs, ρ_G , is given by³⁸

$$\rho_G = \frac{4Y}{bD}, \quad (9)$$

where Y is the average shear strain over an indentation size, D .

Hardness can, therefore, be estimated as

$$H \approx \mu b [\rho_S + \rho_G]^{\frac{1}{2}} = \mu b \left[\rho_S + \frac{4Y}{bD} \right]^{\frac{1}{2}}, \quad (10)$$

where ρ_S is the density of statistically stored dislocations (SSDs) and ρ_G is the density of geometrically necessary dislocations (GNDs). This model shows that the hardness is inversely related to the indent size, D .

Elmstafa *et al.*³⁹ showed that the Taylor hardening model of dislocation can simply be modified as

$$\frac{H^2}{C_1^2} = \frac{\rho_S}{C_2} + \frac{1}{D} \quad (11)$$

with $C_1 = 2 \mu \sqrt{3bY}$ and $C_2 = \frac{4Y}{b}$.

The yield strength/stress, σ_0 , is also affected by the grain size. The grain size dependence is given by the Hall-Petch relationship. The yield strength can be estimated from Tabor's relation,³⁷ which gives $H_0 = 3\sigma_0$. Hence, the Hall-Petch relationship⁴⁰ can be expressed as

$$\sigma_0 = \sigma_{0i} + \frac{k_y}{\sqrt{d}}, \quad (12)$$

where σ_{0i} and k_y are the intrinsic yield strength in the absence of grain size effects and material constant, respectively.

III. MATERIALS AND METHODS

A. Materials

Etched Fluorine-doped Tin Oxide (FTO)-coated glass ($\sim 7 \Omega \text{ sq}^{-1}$) was purchased from MSE Supplies, Tucson, AZ, USA. Lead iodide (PbI_2) (99.999%), di-isopropoxide bis(acetylacetonate), formamidinium iodide (FAI) (98%), methylammonium chloride (MACl), methylammonium bromide (MABr) (98%), dimethylformamide (DMF), dimethylsulfoxide (DMSO), titania paste, 1-butanol, ethanol, iso-propyl alcohol (IPA), 4-tert-butylpyridine (tBP), acetonitrile, lithium bis(trifluoromethylsulfonyl) imide (Li-TFSI), 2, 2', 7,7'-tetrakis (N,N-di-p-methoxyphenylamine)-9,9'-spirobifluorene (Spiro-OMeTAD), and anhydrous chlorobenzene

were all purchased from Sigma-Aldrich (Natick, MA, USA). All the materials were used in their as received conditions.

B. Materials processing

The etched FTO glasses were cleaned with detergent and deionized water. They were sonicated for 15 min successively in deionized water, acetone (Sigma-Aldrich), and IPA (Sigma-Aldrich). The cleaned glass substrates were blown to dry up in nitrogen gas, and UV-ozone cleaning (Novascan, Main Street Ames, IA, USA) was used to remove the organic residues.

According to the preceding protocol,⁴¹ the electron transporting layer (ETL) made of the compact titanium oxide (c-TiO₂) and mesoporous titanium oxide (m-TiO₂) was deposited on the FTO glasses. The compact titanium oxide (c-TiO₂) was spin coated onto the cleaned FTO glass from a 0.15 M solution of titanium diisopropoxide bis(acetylacetonate) in 1-butanol at 2000 rpm for 30 s. This was then annealed at 150 °C for 5 min before spin coating a 0.3 M solution of titanium diisopropoxide bis(acetylacetonate) in 1-butanol at 2000 rpm for 30 s. The deposited c-TiO₂ was then sintered in a furnace (Linberg Blue M, Thermo Fisher Scientific) at 500 °C for 30 min. When the layer cooled down to room temperature, a mesoporous titanium oxide [from a mixture of titania paste and ethanol in the ratio of 1:5 (w:w)] was spin coated onto it at 4000 rpm for 30 s and sintered at 500 °C for 1 h in the furnace (Linberg Blue M, Thermo Fisher Scientific). A mixture of 0.5993 g of PbI₂ and DMF:DMSO (9.5:0.5; v:v) was used to prepare lead iodide solution, which was stirred at 500 rpm for 2 h at 60 °C heating temperature. The mixture was filtered through a 0.45 μm mesh before spin coating onto mesoporous TiO₂ at 1500 rpm for 30 s. The film was annealed at 70 °C for 1 min and allowed to cool down to room temperature.

The formamidinium iodide-rich (FAI-rich) organic solution was then prepared from 60 mg of FAI, 6 mg of MABr, and 6 mg of MACl in 1 ml of IPA. The solution was spin coated onto the PbI₂ layers at 1300 rpm for 30 s. The films were annealed at various temperatures (80, 100, 130, 150, and 170 °C) to form the perovskite layer. Some of the annealed perovskite films were set aside for characterization, while a hole transport layer (HTL) was spin coated on the films for PSC devices.

The HTL was prepared by first dissolving 260 mg of Li-TFSI in 1 ml of acetonitrile. Then, 72 mg of Spiro-OMeTAD was dissolved in 1 ml of chlorobenzene before adding 30 and 35 μl of tBP and Li-TFSI solutions, respectively. The mixture was sonicated for 5 min and spin coated onto the perovskite films at 4000 rpm for 30 s. Finally, a 90 nm thick layer of gold was thermally evaporated onto the films using an Edward E306A thermal evaporator (Edward E306A, Easton PA, USA). The evaporation was carried out at a vacuum pressure of $\sim 1 \times 10^{-6}$ Torr and a deposition rate of 0.2 nm s⁻¹. A shadow mask of 0.12 cm² was used to define the area of the device.

Nanoindentation tests were carried out using the KLA iMicro nanoindentation testing system (Nanomechanics, Inc., Oak Ridge, TN), a universal nanomechanical *in situ* testing platform powered by the InForce 1000 electromagnetic actuator and capacitive displacement sensor. An Avantes UV-vis spectrophotometer (Avantes, BV, USA) was used to measure the optical absorbance of the perovskite films that were annealed at different temperatures. The

microstructures of the top surfaces and cross sections of the films were observed under a field emission gun scanning electron microscope (SEM) (JSM 7000F, JOEL Ltd., Tokyo, Japan). The surface topographies of the films were examined using an atomic force microscope (AFM) (-NX 20 Park Systems, Santa Clara, CA, USA). An x-ray diffractometer (XRD) (Malvern PANalytical, Westborough, MA, USA) was used to obtain the XRD patterns of the perovskite film under a Cu K_{α} radiation source with the beta nickel filter at 40 KV and 40 mA.

For all the perovskite solar cell (PSC) devices produced at different annealing temperatures, the current density–voltage curves were measured using a Keithley sourcemeter unit 2400 system (Keithley, Tektronix, Newark, NJ, USA) connected to an Oriol solar simulator (Oriol, Newport Corporation, Irvine, CA, USA). The devices were exposed to AM 1.5 G illumination of 100 mW cm^{-2} during the current density–voltage measurements. The solar simulator was calibrated using a calibrated silicon cell (91 150 V silicon reference cell, Newport).

C. Nanoindentation experiments

To measure the mechanical properties of the perovskite films, indentation tests on fused silica were performed to acquire the area function calibration. The calibrating method assumes that Young's modulus of elasticity is unaffected by indentation depth.³⁰ For silica used in the calibration experiment, $E_r = 68.6 \text{ GPa}$. The elastic modulus for the Berkovich indenter is 1140 GPa . The Poisson's ratios for the silica and the indenter are 0.17 and 0.07, respectively. A projected contact area was estimated for each indent using Eq. (2). The computed area was then plotted against contact depth (Fig. 1), and a fitting procedure was employed to fit A vs h_c to a polynomial from Eq. (5). Using this approach, the coefficients C_1 through C_8 have been calibrated for the Berkovich indenter used in the current study.

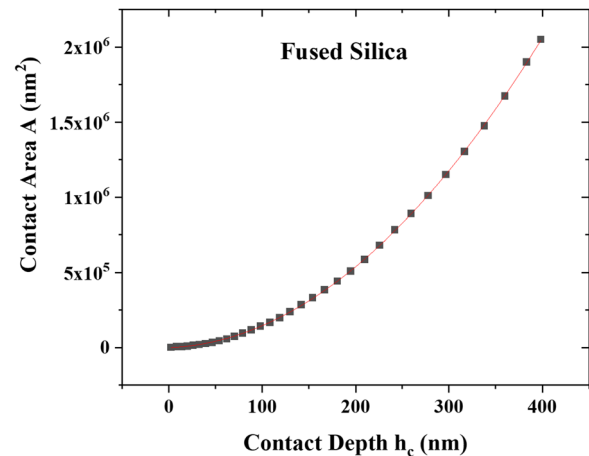


FIG. 1. The computed projected contact area A as a function of contact depth h_c with a polynomial fit.

After the calibration, nano-indentation experiments were performed on the perovskite films annealed at 80, 100, 130, 150, and 170 °C.

The nanoindentation experiments were carried out with the iMicro, a universal nanomechanical *in situ* testing platform powered by the InForce 1000 electromagnetic actuator and capacitive displacement sensor (Nanomechanics, Inc., Oak Ridge, TN) using the dynamic constant strain rate (CSR) for thin films test method. The indenter used was a diamond Berkovich indenter with a tip radius of 20 nm. The indenter was brought into contact with the film at a speed of 100 nm/s and a surface approach distance of 2000 nm. While oscillating at a frequency of 100 Hz with an amplitude of 1 nm, the indenter was driven into the film's surface at a strain rate of 0.2/s

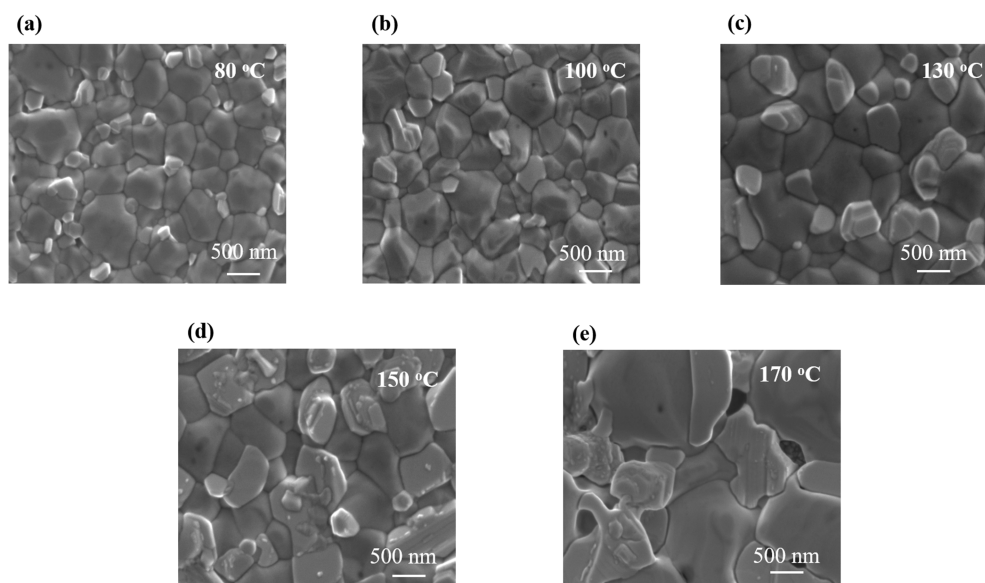


FIG. 2. SEM images of perovskite layers annealed at (a) 80 °C, (b) 100 °C, (c) 130 °C, (d) 150 °C, and (e) 170 °C.

to 40% of the film thickness. At least 64 experimentally valid indentations were done per sample using a separation of 60 μm between two adjacent indentation sites to reduce the possibility of indentation interactions. For each indent, a load–displacement curve was recorded.

In this analysis, the Berkovich diamond indenter properties E_i and ν_i used are 1140 GPa and 0.07, respectively. The film's substrate has been shown to have a considerable impact on estimates of the Young's modulus obtained using nanoindentation.³² The film–substrate model by Hay and Crawford was used to eliminate the effects of the FTO glass substrate on the perovskite films. The model's inputs include the film thickness, Poisson's ratio of the film, and the substrate's elastic characteristics. The input values used in this work are as follows: film thickness = 500nm, $\nu_f = 0.33$, $E_s = 105\text{GPa}$, and $\nu_s = 0.4$.

IV. RESULTS AND DISCUSSION

A. Microstructure of perovskite films

The perovskite films were processed and observed under SEM. Figures 2(a)–2(e) represent the SEM microstructural images of the perovskite film annealed at 80 and 170 $^{\circ}\text{C}$. We estimated the grain size values from SEM images of several perovskite films that were processed at different annealing temperatures. The SEM images were analyzed using ImageJ software (ImageJ, National Institutes of Health, Bethesda, MD, USA). The average roughness values were estimated from AFM images that were analyzed using Gwyddion software. To the best of our knowledge, the values were obtained accurately. The results show that the size of the grain increases with increasing annealing temperature. Similar trends have been reported in prior work.^{16,19}

The average grain size estimated increased from 493.0 ± 135.4 to 1616.0 ± 457.3 nm, as the annealing temperature increased from

TABLE I. Grain size d and surface roughness values.

Temp ($^{\circ}\text{C}$)	Grain size d (nm)	Surface roughness (nm)
80	493.1 ± 135.4	41.3 ± 3.0
100	515 ± 154.5	35.8 ± 0.5
130	677 ± 206.2	38.0 ± 2.5
150	808 ± 228.3	40.4 ± 3.1
170	1616 ± 457.3	73.7 ± 8.0

80 to 170 $^{\circ}\text{C}$. The estimated grain size is summarized in Table I. A smooth compact perovskite film layer was obtained as the annealing temperature increased to 130 $^{\circ}\text{C}$ [Figs. 2(b) and 2(c)]. Lower annealing temperature (80 $^{\circ}\text{C}$) yielded rough films with pinhole-like defects [Fig. 2(a)]. For the films annealed at higher temperature, the film rapidly crystallized to form larger grains [Figs. 2(d) and 2(e)], which resulted in formations of defects (void and cracks) along the grain boundaries [Fig. 2(e)].

Large and irregularly shaped plate-like grains were observed in perovskite films annealed at 150 $^{\circ}\text{C}$. The films were also rougher and had bigger grain sizes than those observed in perovskite films annealed at lower temperatures. Larger grains with voids between them were also observed in the films annealed at 170 $^{\circ}\text{C}$. The rapid growth of grains from a few nucleation sites was also associated with void formation¹⁹ and significant reductions in solar cell performance.

Contact mode atomic force microscopy (AFM) was used to characterize the surface roughness of the perovskite films. Typical AFM images of the films annealed at different temperatures between 80 and 170 $^{\circ}\text{C}$ are presented in Fig. 3. The 3D orientations of the

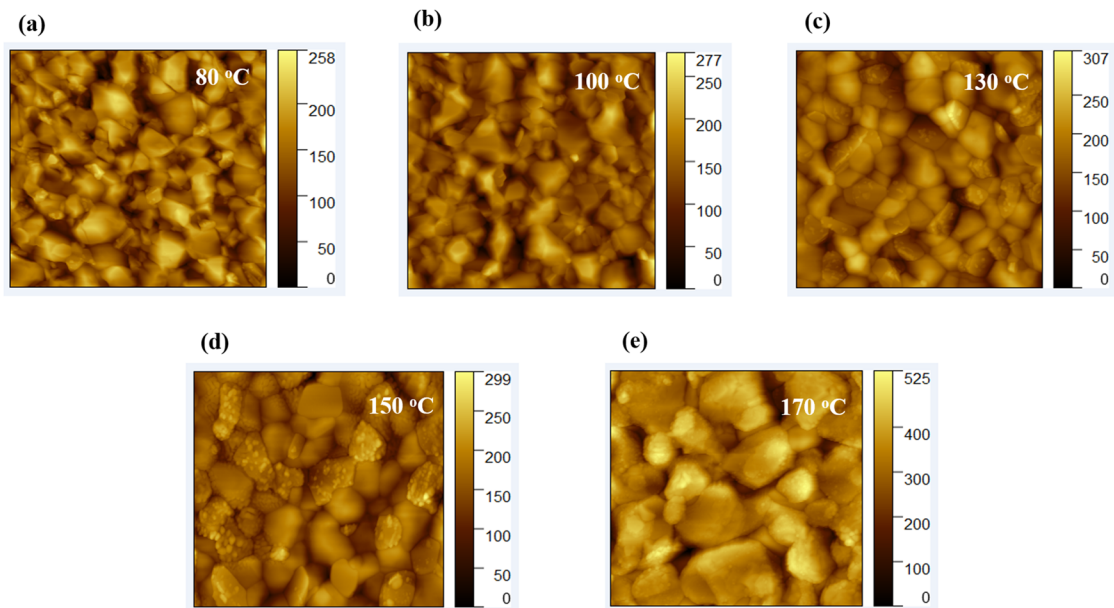


FIG. 3. Typical AFM images of the perovskite films annealed at (a) 80 $^{\circ}\text{C}$, (b) 100 $^{\circ}\text{C}$, (c) 130 $^{\circ}\text{C}$, (d) 150 $^{\circ}\text{C}$, and (e) 170 $^{\circ}\text{C}$.

TABLE II. Summary of the Young's modulus and hardness values for perovskite films annealed at different temperatures.

Temp (°C)	E (GPa)	H (GPa)
80	12.4 ± 1.1	0.822 ± 0.103
100	12.9 ± 1.3	0.813 ± 0.107
130	13.2 ± 1.2	0.828 ± 0.112
150	12.6 ± 1.5	0.751 ± 0.146
170	10.4 ± 1.7	0.54 ± 0.144

AFM images are presented in Fig. S1. The AFM images show the equiaxed grain structures in the deposited films. The surface roughness data that were obtained for the perovskite films are summarized in Table I. The results showed that the average surface roughness values of the films annealed at a very high temperature are higher, indicating the presence of large pinholes and grain boundary voids [Fig. 2(e)]. The results are consistent with prior studies of the film microstructure, which show that surface roughness increased with annealing temperature.⁴²

B. Mechanical properties of perovskite films

The Young's moduli and hardness of the perovskite films annealed at different temperatures are summarized in Table II. The hardness value for films annealed between 80 and 130 °C is ~0.82 GPa. The hardness values for the films annealed above 130 °C decreased to 0.75 and 0.54 GPa for films annealed at 150 and 170 °C. The hardness values decrease by increasing temperature to 150 °C. This is attributed to interactions between dislocations and more widely spaced grain boundaries that occur at temperatures of up to 150 °C. However, above 150 °C, the occurrence of recrystallization (smaller grains) and micro-voids results in a reduction of hardness after annealing at higher temperatures.^{19,43,44}

The Young's modulus value slightly increased from 12.4 to 13.2 GPa for films annealed between 80 and 130 °C and decreased to 12.6 and 10.4 GPa for films annealed at 150 and 170 °C. The representative load–displacement curves for the film annealed at different temperatures are shown in Fig. 4(a). The plots of Young's modulus vs depth obtained for each of the perovskite films annealed between

TABLE III. Micro- and nano-length scales for different annealing temperatures.

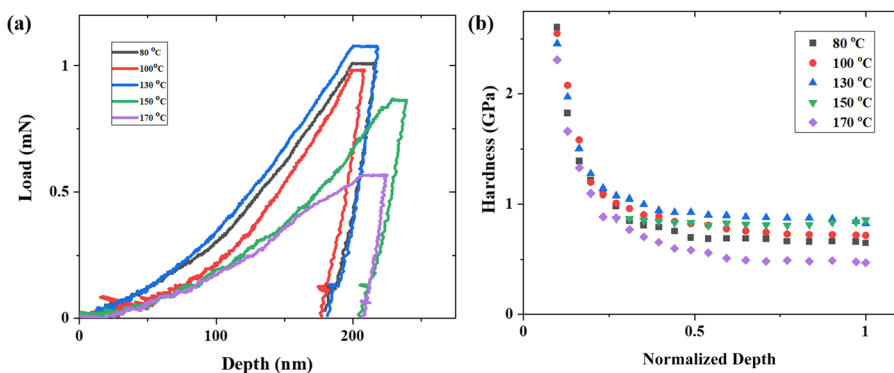
Temp (°C)	Micro-scales (μm)	Nano-scales (μm)
80	4.52	6.59
100	3.77	3.85
130	1.80	1.72
150	2.97	2.68
170	360.89	34.94

80 and 170 °C are presented in Figs. S2(a)–S2(e). The obtained Young's moduli of 10.4–13.2 GPa and hardness values of 0.54–0.83 GPa are in reasonable agreement with prior reports.²⁴ Ma *et al.*²³ also presented Young's moduli and hardness values of 11.5–19.2 GPa and 0.047–0.63 GPa, respectively.

C. Indentation size effects

Figure 4(b) represents the contact depth dependence of hardness obtained for all the perovskite films annealed at different temperatures. Indentation size effects (ISEs), a phenomenon in which the measured hardness values increase with decreasing indentation depth, were observed in all the film tested. This is because of the effects of geometrically necessary dislocations at a small scale.²⁸ The hardness values increase at both the micro- and nano-scales as the indentation depth reduces [Fig. 4(b)]. The level of the increase at the nanoscale, however, is much more than that at the microscale. The ISE for films annealed at different annealing temperatures is presented in Figs. S3(a)–S3(e), while the representative images of the indents are presented in Figs. S4(a)–S4(c). The indents are typically on grains within the perovskite films (Fig. S4), with pileup occurring in some cases [Fig. S4(c)].

To relate the indentation size dependence of hardness to the strain gradient, the intrinsic material length scale \hat{l} was calculated using a mechanism-based strain gradient (MSG) model [Eq. (8)]. The shear modulus μ value of 6.37 GPa⁴⁵ and Burger's vector b of 0.2995 nm were used. The characteristic length scale \hat{l} of the material measures how much the stress gradient contributes to the plasticity. The intrinsic length scales for the films at different annealing the temperatures are summarized in Table III.

**FIG. 4.** (a) The load–displacement curves for the film annealed at different temperatures and (b) hardness–depth curves.

Micro-length scales between 2.97 and 4.52 μm and nano-length scales between 2.68 and 6.59 μm were obtained for annealing temperatures between 80 and 150 $^{\circ}\text{C}$. In the case of the films prepared at 170 $^{\circ}\text{C}$ annealing temperature, 360.89 and 34.94 μm of micro- and nano-length scales were obtained, respectively. The values obtained are close to the value range of 1.15–6.51 μm reported by Zong *et al.* for the nanoscale⁴⁶ and ~ 12 and 6 μm , respectively, reported for annealed copper and work-hardened copper by Nix and Gao.³⁶ The measured values of \hat{l} decreased as the annealing temperature increases. Larger values of \hat{l} indicate greater spacing between statistically stored dislocations. This could lead to weaker dislocation interactions and lower intrinsic strengthening of films annealed at higher temperatures.

The density of geometrically necessary dislocations (GNDs), ρ_G , was computed from Eq. (9), and the hardness values were estimated from Eq. (10). This model shows that the square of hardness is inversely related to the indent size, D . The values of the density of statistically stored dislocations (SSDs) ρ_s and shear strain γ were obtained by fitting the experimental data into Eq. (10). The estimated values of ρ_s : 108–197 μm^{-2} , ρ_G : 0.6–1.9 μm^{-2} , and γ : 13.1%–21.1% that were obtained for the different annealing temperatures are summarized in Table IV. Similar values of 389–543 μm^{-2} for ρ_s and 10%–21% for γ have been reported in prior studies for single crystal metals by Tong *et al.*⁴⁴ The plots of ρ_G vs the inverse of the indentation depth D^{-1} , within the nanoscale, are presented in Fig. 5(a) for perovskite films annealed at different temperatures.

The density of GNDs increases with decreasing indentation depth. Since the SSDs varied slightly in the films annealed at different temperatures, an explanation for the size effect is that the increase in ρ_G is connected to the increasing strain gradients at small scales. The increased hardness is due to the increased interactions

TABLE IV. Estimates of average shear strain, GND, and SSD densities.

Temp ($^{\circ}\text{C}$)	ρ_s (μm^{-2})	$\rho_G \times 10^5$ (μm^{-2})	γ (%)
80	108.5	1.85	18.7
100	126.8	1.81	19.9
130	196.6	1.89	20.1
150	142.7	1.54	21.5
170	141.8	0.63	13.1

between the closer spaced GNDs at small scales. These interactions cause hardening and strong indentation size effects in the nano- and microscales. Other researchers have reported similar indentation size dependence on hardness.^{36,47–49} The difference in the curve for 80 $^{\circ}\text{C}$ [Fig. 5(a)] compared to the rest of the annealing temperatures can be associated with texture and crystallinity of the films.

A plot of the square of hardness against the reciprocal of the indentation depth in Eq. (11) gives a linear relationship for data at both micro- and nano-scales [Figs. S5(a)–S5(e)] but with different slopes for the micro-hardness and nano-hardness data. The results in the nano- and micro-scales constitute a bi-linear indentation size behavior.³⁹ For an average indentation size of 100 nm in the nanoscale for the 80 $^{\circ}\text{C}$ annealing temperature, the density for GNDs calculated from Eq. (9) is $\sim 2.4 \times 10^{16} \text{ m}^{-2}$. At the micro-scale, for an average indentation size of 100 μm , the density for GNDs calculated is $\sim 2.4 \times 10^{13} \text{ m}^{-2}$. Hence, the average dislocation spacing L ($L = 1/\sqrt{\rho_G}$) for the film annealed at 80 $^{\circ}\text{C}$ is $\sim 6.45 \text{ nm}$ for a nano-indentation of $\sim 100 \text{ nm}$ and $\sim 0.204 \mu\text{m}$ for a micro-indentation size of 100 μm .

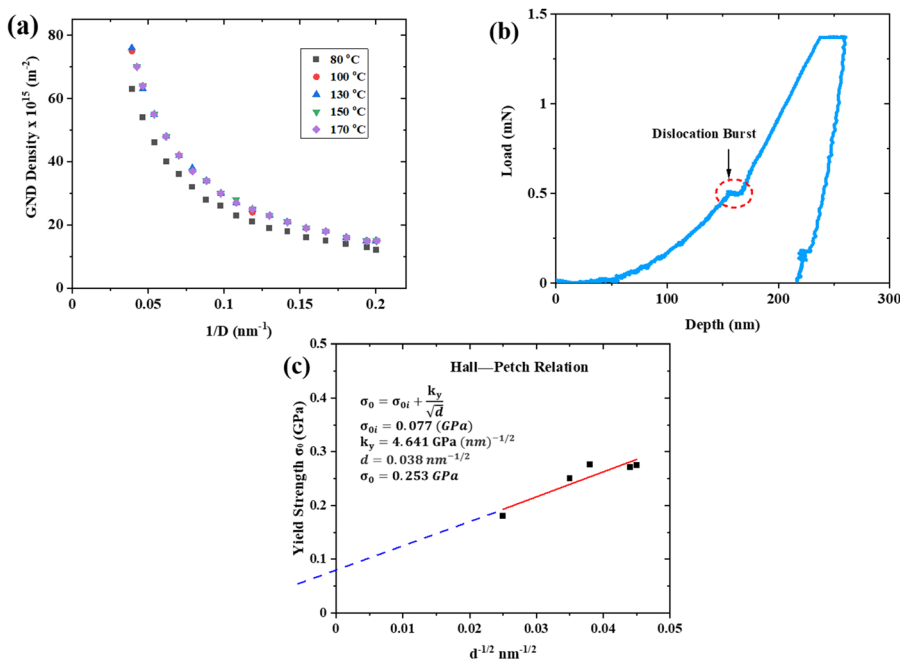


FIG. 5. (a) Plots of GND density ρ_G vs inverse of the indentation depth D^{-1} . (b) Dislocation burst on the load-displacement curve of the perovskite film annealed at 80 $^{\circ}\text{C}$. (c) Plot of σ_0 vs $d^{-1/2}$ with the linear fit for perovskite films annealed at different temperatures.

Consequently, only relatively few GND rows are introduced into the deformed regions for an indentation size of ~ 100 nm. Multiple dislocations must be initiated to compensate for these dislocation source limited conditions. At such dislocation starved conditions, very high stresses nucleate new dislocations, leading to the observed high strengths.⁴⁹ Furthermore, the discrete displacement bursts found during the initial period of nano-indentation in perovskite films are possible evidence of nucleation dislocations.⁴⁷ Typical displacement dislocation burst is seen in the film annealed at 80 °C [Fig. 5(b)].

At the micro-scale indents, however, there is an established dislocation substructure under the indenter. It is assumed that this has a different plasticity length scale in the micro-scale. Hence, the bi-linear behavior is evidence of the differences in source limited dislocation structures of indentation at the nanoscale and the deformation by established dislocation structures at the sub-microscale and microscale. The different deformation mechanisms also account for the differences in the length scale \hat{l} values at the nano- and microscales.

The film grain size was related to the intrinsic film strength/hardness in the absence of strain gradient plasticity (SGP) phenomena. Figure 5(c) shows the experimental data of σ_0 vs $d^{-1/2}$ and the corresponding linear fit based on Eq. (12). H_0 is linearly related to $d^{-1/2}$. The values of k_y and σ_{0i} (obtained using linear fitting for perovskite film) are 4.64 GPa (nm)^{-1/2} and 0.077 GPa, respectively.

The calculated intrinsic yield strengths for the perovskite films annealed between 80 and 170 °C are presented in Table V. The intrinsic yield strength increases as the annealing temperature increases. This is attributed to the reduction in the grain boundary obstacles per unit volume that occurs with increasing grain sizes at higher annealing temperatures. However, for annealing

TABLE V. Yield strength of the film annealed at different temperatures.

Temp (°C)	$d^{-1/2}$ (nm) ^{-1/2}	σ_0 (GPa)
80	0.045	0.271
100	0.044	0.274
130	0.038	0.276
150	0.035	0.25
170	0.025	0.18

temperatures between 150 and 170 °C, the intrinsic yield strength decreased due to the effects of recrystallization and microvoid formation.^{21,43,50} Yield strength values of 0.133–0.181 GPa have been previously reported for MAPbI₃.²¹

D. Optical and structural properties

The absorption spectra are presented in Fig. 6(a) for the perovskite films that are prepared at different annealing temperatures. The absorption increased by increasing annealing temperature from 80 to 130 °C [Fig. 6(a) (top)], while the light absorption is reduced as the annealing temperature is raised further from 150 to 170 °C [Fig. 6(a) (bottom)]. The increase in the absorbance, for the films annealed between 80–130 °C, is associated with the increased grain size (Table I). The increase in the grain size is due to tensile strain in the film, which can, therefore, leads to compressive strain along the grain boundaries due to the increasing annealing temperature from 80 to 170 °C. The observed decrease in the absorbance peaks for the films annealed at 150 and 170 °C is associated with the initiation of grain boundary cracks [Fig. 2(e)], which is driven by the

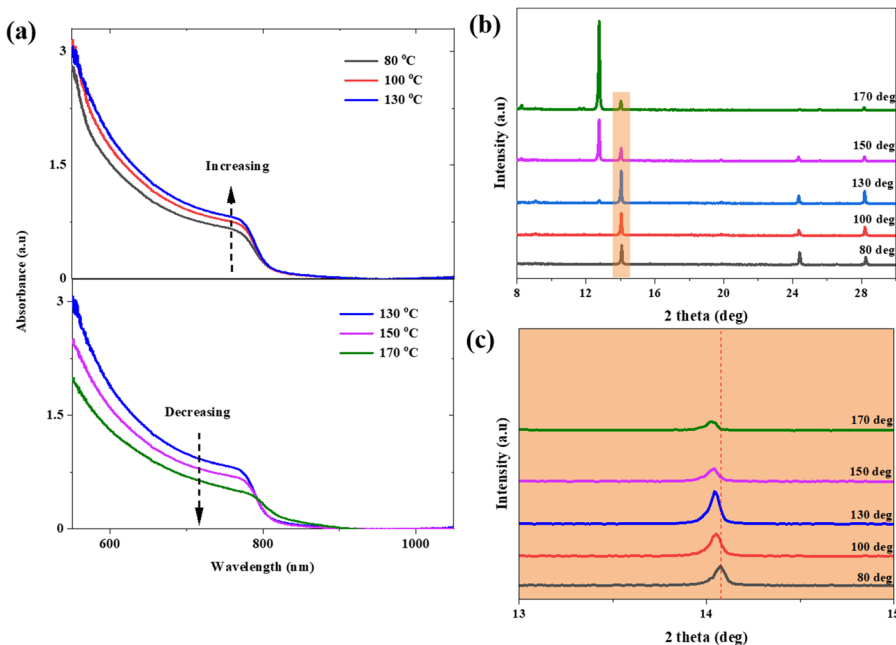


FIG. 6. (a) Absorption spectral of films, showing an increase in the absorbance by increasing annealing temperatures from 80 to 130 °C (top) and a decrease between 130 and 170 °C (bottom). (b) XRD patterns of films annealed at different temperatures. (c) Magnified XRD patterns of the α -phase of the perovskite films annealed at different temperatures.

strains along the grain boundaries. The tensile strains in the perovskite films have been presented earlier¹⁹ for different annealing temperatures.

To further elucidate the effects of annealing temperature on the structure and crystallinity, we used the x-ray diffractometer (XRD) to produce x-ray diffraction patterns of the perovskite films. Figure 6(b) represents the XRD patterns of the samples. The results show that the films have strong and sharp diffraction peaks, indicating high crystallinity for the cubic perovskite phase. The crystallinity of the samples increased as the annealing temperature increased from 80 to 130 °C as shown by the strong and sharp diffraction peaks. At higher temperatures between 150 and 170 °C, the crystallinity of the samples reduces, as evident in the reduced diffraction peaks [Fig. 6(b)]. The diffraction peak at a 2θ value of $\sim 14^\circ$ observed from perovskite films suggests the presence of a pure α -perovskite phase.⁵¹ The intensity of the peak increases with the increasing annealing temperature between 80 and 130 °C [Fig. 6(b)]. The diffraction patterns obtained for the films annealed at temperatures above 130 °C show a reduction of the α -phase of perovskites. This suggests that the α -phase has been converted to cubic PbI_2 [Fig. 6(b)]. The cubic PbI_2 phase is more pronounced at 170 °C, indicating that at higher temperatures, most of the perovskite film decomposes to PbI_2 .

Annealing of the double cation (FA and MA) mixed halide organic components and PbI_2 produces a dark brown cubic

perovskite phase,¹⁹ as the annealing temperature rises from 80 to 130 °C. At higher temperatures between 150 and 170 °C, a hexagonal perovskite phase is formed,¹⁹ which is evident in the PbI_2 peak at 130 °C with intensity being higher for the films annealed at 150 and 170 °C. Furthermore, a shift to lower diffraction angles was also observed in the perovskite films [Fig. 6(c)]. This shift indicates tensile strain in the perovskite films⁵² due to lattice expansion that can cause compressive strains at the grain boundaries. The 2θ values of 14° , 24.4° , and 28.2° correspond, respectively, to (110), (111), and (220) lattice planes for the perovskite tetragonal phase.^{44,53,54}

E. Electrical properties of PSCs

To further understand the effects of annealing temperature on the mechanical properties of PSCs, we characterize the current–voltage characteristics of the devices fabricated at different annealing temperatures. Figure 7(a) shows that the current density–voltage curves of PSCs prepared at annealing temperatures range between 80 and 170 °C. The architecture of the device is presented in Fig. 7(a) (inset). For the films annealed between 80 and 130 °C, we observed an increase in the hardness (H), open-circuit voltage (V_{oc}), short circuit current density (J_{sc}), and power conversion efficiency (PCE) [Figs. 7(b)–7(e)]. From 80 to 130 °C, the devices exhibit improved performance characteristics with increasing hardness of the perovskite film. However, the

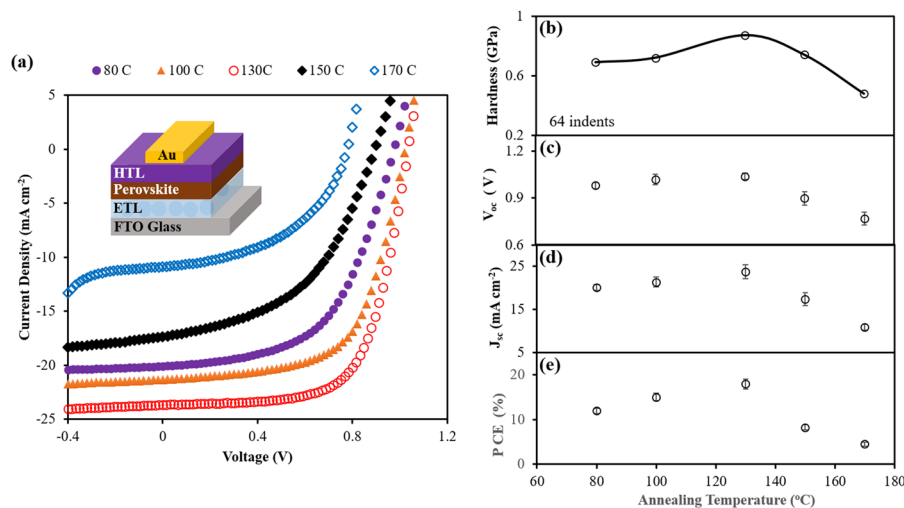


FIG. 7. Effects of annealing temperature on performance and mechanical properties. (a) J–V curves with the schematic of the device architecture (inset). (b) Hardness vs temperature. (c) Open circuit voltage. (d) Current density. (e) PCE of the PSCs at different annealing temperatures.

TABLE VI. Summary of device parameters at different annealing temperatures.

Device parameter	Annealing temperature (°C)				
	80	100	130	150	170
V_{oc} (V)	0.980 (0.89 ± 0.021)	1.019 (0.991 ± 0.032)	1.039 (1.002 ± 0.022)	0.899 (0.786 ± 0.043)	0.768 (0.678 ± 0.042)
J_{sc} (mA cm ²)	20.08 (19.32 ± 1.34)	21.31 (19.56 ± 2.31)	23.67 (21.54 ± 3.23)	17.35 (15.89 ± 3.02)	10.88 (8.81 ± 1.27)
FF	0.549 (0.510 ± 0.012)	0.625 (0.594 ± 0.021)	0.658 (0.641 ± 0.023)	0.478 (0.421 ± 0.013)	0.484 (0.436 ± 0.041)
PCE (%)	11.99 (10.43 ± 1.20)	15.07 (14.23 ± 1.74)	17.98 (16.02 ± 2.32)	8.28 (7.04 ± 1.24)	4.50 (3.89 ± 0.89)

hardness values of the perovskite films and the device parameters decreased with a further increase in the annealing temperature [Figs. 7(b)–7(e)]. The device parameters are summarized in Table VI.

It is important to note that the mechanical properties of films and device performance characteristic parameters show a clear relation with the increasing annealing temperature. The increased annealing temperature results in improved PCEs due to increased grain size and inter-diffusion of materials between layers in the PSCs,¹⁹ while the increased hardness is due to a thermal-induced decrease in material length scales (Table III) and yield strength (Table V).

As the annealing temperature increases from 80 to 130 °C, the crystallinity of the sample increases, and we observed an increase in the hardness (H), open-circuit voltage (V_{oc}), short circuit current density (J_{sc}), and power conversion efficiency (PCE) [Figs. 7(b)–7(e)]. From 80 to 130 °C, the devices exhibit improved performance characteristics. However, the device parameters decreased with a further increase in the annealing temperature between 150 and 170 °C with a reduction in the hardness (H), open-circuit voltage (V_{oc}), short circuit current density (J_{sc}), and power conversion efficiency (PCE). The J–V curves also show the presence of some resistances in the devices due to voids and cracks. At the higher temperatures (150 and 170 °C), the defects caused by voids and cracks decreased the PCE values, and increased length scale values lowered the hardness of the films. The best performing devices are those annealed at 130 °C and have a PCE of 17.98% and a hardness value of 0.83 GPa.

V. SUMMARY AND CONCLUDING REMARKS

We have shown that the temperature at which the perovskite film is annealed affects the mechanical properties of the devices fabricated. The size dependence of hardness is due to the increase in the density of GNDs with decreasing indentation size. The indentation size effects are characterized between the microscale- and nano-scale by a bi-linear SGP framework with source-limited and established dislocation substructures. The measured microstructural length scales decrease by increasing the annealing temperature to 130 °C, after which it began to increase, causing films annealed beyond 130 °C to have reduced strengths because the larger microstructural length scales correspond to larger dislocation spacings and weaker dislocation interactions. Perovskite solar devices annealed at temperatures above 130 °C have poor performance. We have shown that perovskite solar cell devices annealed at 130 °C exhibit optimal performance and attractive combinations of mechanical properties.

SUPPLEMENTARY MATERIAL

See the [supplementary material](#) for additional figures of the 3D orientations of the AFM images of the films that were annealed at different temperatures, film modulus vs depth for perovskite films annealed at different temperatures, film hardness vs depth for perovskite films annealed at different temperatures, SEM images of indents on grains of the perovskite films, and the bi-linear behavior from micro- to nano-scale for perovskite films annealed at different temperatures.

ACKNOWLEDGMENTS

This research was supported by the grants from the Pan African Materials Institute (PAMI) of the African Centers of Excellence Program (Grant No. P126974) and Worcester Polytechnic Institute. The authors acknowledge the African University of Science and Technology (AUST) for their financial support.

AUTHOR DECLARATIONS

Conflict of Interest

The authors declare that they have no conflict of interest.

DATA AVAILABILITY

The data that support the findings of this study are available from the corresponding author upon reasonable request.

REFERENCES

- 1 S. D. Stranks, and H. J. Snaith, *Nat. Nanotechnol* **10**, 391 (2015).
- 2 S. G. R. Bade, J. Li, X. Shan, Y. Ling, Y. Tian, T. Dilbeck, *et al.*, *ACS Nano* **10**, 1795 (2015).
- 3 Y. Fu, H. Zhu, A. W. Schrader, D. Liang, Q. Ding, P. Joshi, *et al.*, *Nano Lett* **16**, 1000 (2016).
- 4 NREL, “National Renewable Energy Laboratory Photovoltaic Research: Best Research-Cell Efficiency Chart. *Best Research-Cell Efficiency Chart: Photovoltaic Research*,” NREL (2020).
- 5 E. Mosconi, P. Umari, and F. De Angelis, *J. Mater. Chem. A* **3**, 9208 (2015).
- 6 X. Mettan, R. Pisoni, P. Matus, A. Pisoni, J. Jaćimović, B. Náfrádi, *et al.*, *J. Phys. Chem. C* **119**, 11506 (2015).
- 7 M. Cheng, Y. Li, M. Safdari, C. Chen, P. Liu, L. Kloo, and L. Sun, *Advanced Energy Materials* **7**, 1602556 (2017).
- 8 M. A. Green, A. Ho-Baillie, and H. J. Snaith, *Nat. Photonics* **8**, 506 (2014).
- 9 M. Grätzel, *Nat. Mater* **13**, 838 (2014).
- 10 G. Lee, M.-c. Kim, Y. W. Choi, N. Ahn, J. Jang, J. Yoon, *et al.*, *Energy Environ. Sci* **12**, 3182 (2019).
- 11 M. Park, H. J. Kim, I. Jeong, J. Lee, H. Lee, H. J. Son, *et al.*, *Adv. Energy Mater* **5**, 1501406 (2015).
- 12 M. Kim, G.-H. Kim, K. S. Oh, Y. Jo, H. Yoon, K.-H. Kim, *et al.*, *ACS Nano* **11**, 6057 (2017).
- 13 T. Su, X. Li, Y. Zhang, F. Zhang, and Z. Sheng, *Phys. Chem. Chem. Phys* **19**, 13147 (2017).
- 14 W. Peng, B. Anand, L. Liu, S. Sampat, B. E. Bearden, A. V. Malko, and Y. J. Chabal, *Nanoscale* **8**, 1627 (2016).
- 15 X. Cao, L. Zhi, Y. Jia, Y. Li, X. Cui, K. Zhao, *et al.*, *J. Colloid Interface Sci* **524**, 483 (2018).
- 16 L.-C. Chen, J.-R. Wu, Z.-L. Tseng, C.-C. Chen, S. H. Chang, J.-K. Huang, *et al.*, *Materials* **9**, 747 (2016).
- 17 A. Dualeh, N. Tétreault, T. Moehl, P. Gao, M. K. Nazeeruddin, and M. Grätzel, *Adv. Funct. Mater* **24**, 3250 (2014).
- 18 C. Wehrenfennig, M. Liu, H. J. Snaith, M. B. Johnston, and L. M. Herz, *APL Mater* **2**, 081513 (2014).
- 19 D. O. Oyewole, R. K. Koech, R. Ichwani, R. Ahmed, J. Hinostroza Tamayo, S. A. Adeniji, *et al.*, *AIP Adv* **11**, 065327 (2021).
- 20 J. Feng, *APL Mater* **2**, 081801 (2014).
- 21 J. Yu, M. Wang, and S. Lin, *ACS Nano* **10**, 11044 (2016).
- 22 Y. Rakita, S. R. Cohen, N. K. Kedem, G. Hodes, and D. Cahen, *MRS Commun* **5**, 623 (2015).
- 23 L. Ma, W. Li, K. Yang, J. Bi, J. Feng, J. Zhang, *et al.*, *APL Mater* **9**, 041112 (2021).
- 24 S. Sun, F. H. Isikgor, Z. Deng, F. Wei, G. Kieslich, P. D. Bristowe, *et al.*, *ChemSusChem* **10**, 3740 (2017).

- ²⁵M. A. Reyes-Martinez, A. L. Abdelhady, M. I. Saidaminov, D. Y. Chung, O. M. Bakr, M. G. Kanatzidis, *et al.*, *Adv. Mater.* **29**, 1606556 (2017).
- ²⁶K. Poorkazem, D. Liu, and T. L. Kelly, *J. Mater. Chem. A* **3**, 9241 (2015).
- ²⁷M. Faghihnasiri, M. Izadifard, and M. E. Ghazi, *J. Phys. Chem. C* **121**, 27059 (2017).
- ²⁸H. Gao, Y. Huang, W. D. Nix, and J. W. Hutchinson, *J. Mech. Phys. Solids* **47**, 1239 (1999).
- ²⁹Q. Ma, and D. R. Clarke, *J. Mater. Res* **10**, 853 (1995).
- ³⁰W. C. Oliver, and G. M. Pharr, *J. Mater. Res* **7**, 1564 (1992).
- ³¹J. Hay, and B. Crawford, *J. Mater. Res* **26**, 727 (2011).
- ³²M. F. Doerner, and W. D. Nix, *J. Mater. Res* **1**, 601 (1986).
- ³³J. Lou, P. Shrotriya, T. Buchheit, D. Yang, and W. O. Soboyejo, *J. Mater. Res* **18**, 719 (2003).
- ³⁴R. Saha, and W. D. Nix, *Acta Mater* **50**, 23 (2002).
- ³⁵N. A. Fleck, G. M. Muller, M. F. Ashby, and J. W. Hutchinson, *Acta Metall. Mater* **42**, 475 (1994).
- ³⁶W. D. Nix, and H. Gao, *J. Mech. Phys. Solids* **46**, 411 (1998).
- ³⁷A. G. Quarrell, *Nature* **170**, 818 (1952).
- ³⁸M. F. Ashby, *Philos. Mag* **21**, 399 (1970).
- ³⁹A. A. Elmustafa, J. Lou, O. Adewoye, W. O. Soboyejo, and D. S. Stone, *MRS Online Proc. Libr* **750**, 17 (2002).
- ⁴⁰W. D. Callister, *Rethwisch*, 10th ed., Wiley, (2018).
- ⁴¹O. V. Oyelade, O. K. Oyewole, S. A. Adeniji, R. Ichwani, D. M. Sanni, and W. O. Soboyejo, *Sci Rep* **10**, 7183 (2020).
- ⁴²J.-Q. Chen, Q.-S. Huang, R.-Z. Qi, Y.-F. Feng, J.-T. Feng, Z. Zhang, *et al.*, *Nucl. Sci. Tech* **30**, 107 (2019).
- ⁴³Z. D. Sha, S. S. Quek, Q. X. Pei, Z. S. Liu, T. J. Wang, V. B. Shenoy, and Y. W. Zhang, *Sci. Rep* **4**, 5991 (2014).
- ⁴⁴X. Tong, H. Zhang, and D. Y. Li, *Sci. Rep* **5**, 8459 (2015).
- ⁴⁵L. Guo, G. Tang, and J. Hong, *Chin. Phys. Lett* **36**, 056201 (2019).
- ⁴⁶Z. Zong, J. Lou, O. O. Adewoye, A. A. Elmustafa, F. Hammad, and W. O. Soboyejo, *Mater. Sci. Eng.: A* **434**, 178 (2006).
- ⁴⁷Z. Zong, and W. Soboyejo, *Mater. Sci. Eng.: A* **404**, 281 (2005).
- ⁴⁸Y. Cao, S. Allameh, D. Nankivil, S. Sethiaraj, T. Otiti, and W. Soboyejo, *Mater. Sci. Eng.: A* **427**, 232 (2006).
- ⁴⁹J. R. Greer, and W. D. Nix, *Appl. Phys. A* **80**, 1625 (2005).
- ⁵⁰M. Schneider, F. Werner, D. Langenkämper, C. Reinhart, and G. Laplanche, *Metals* **9**, 84 (2019).
- ⁵¹S. S. Shin, W. S. Yang, J. H. Noh, J. H. Suk, N. J. Jeon, J. H. Park, *et al.*, *Nat. Commun* **6**, 7410 (2015).
- ⁵²C. Zhu, X. Niu, Y. Fu, N. Li, C. Hu, Y. Chen, *et al.*, *Nat. Commun* **10**, 815 (2019).
- ⁵³F. Ma, J. Li, W. Li, N. Lin, L. Wang, and J. Qiao, *Chem. Sci* **8**, 800 (2016).
- ⁵⁴Y. Zhao, and K. Zhu, *J. Phys. Chem. Lett* **4**, 2880 (2013).